International Journal of Materials Engineering 2014, 4(1): 5-24
DOI: 10.5923/j.ijme.20140401.02

Study and Improvement of Thermoelectric Properties of $Ca_3Co_4O_9$/Ag Composite Ceramics

Jérôme Dikwa[1,2,*], Jean-Marie Bienvenu Ndjaka[2], Danwe Raidandi[3], Simon Quetel-Weben[4], Pierre Owono Ateba[2]

[1]College of Technology, The University of Ngaoundere, PO. Box 455 Ngaoundere, Cameroon
[2]Faculty of Science, The University of Yaounde 1, PO. Box 812 Yaounde, Cameroon
[3]National Advanced School of Engineering, The University of Yaounde 1, PO. Box 8390 Yaounde, Cameroon
[4]CRISMAT-ENSICAEN Laboratory, UMR CNRS 6508, 14050 CeanCedex, France

Abstract This study deals with the development and texturing of $Ca_3Co_4O_9$/Ag composites, by substituting Ca^{2+} cations with Ag^+ cations, or by adding massive silver in the $Ca_3Co_4O_9$ phase in order to take advantage of the metallic nature of silver and the effect of texture to optimize the power factor (PF) and the figure of merit (ZT). The conventional method of synthesis reaction in the solid state and the innovative technique of texturing called Spark Plasma Texturing (SPT) that combines both the Spark Plasma Sintering (SPS) method and the oriented nature of Hot Pressing (HP) were used. Microstructural analysis of sintered pellets by SPT shows grains as platelets larger sizes than those of sintered pellets by SPS, and with a preferential orientation perpendicular to the pressing axis. Consequently, we obtained a maximum PF value $555\ \mu W.m^{-1}K^{-2}$ at 900 K, which is among the best reported about textured materials and a time saving of 98% compared to Hot Pressing (HP).

Keywords Oxides, Spark plasma texturing, Microstructure, Anisotropy, Power factor

1. Introduction

The use of materials for thermoelectric conversion typically involves choosing materials with a higher figure of merit ZT [1] or optimizing the dimensionless term (ZT). The figure of merit ZT is defined by $ZT = \frac{\alpha^2}{\rho.\lambda}T = PF \times \frac{1}{\lambda}T$; where α, λ, ρ, PF and T denote respectively the thermopower, thermal conductivity, electrical resistivity, the power factor and the absolute temperature. Under high temperature applications, conventional materials based on telluride, antimony and their derivatives suffer decomposition mainly due to volatilization of certain elements. In this context, oxides, which may have interesting performance combined with chemical and physical stability at higher temperature on air, appear as candidates of great interest. The use of oxides as constituent materials of thermoelectric conversion device has been proposed recently. Indeed, their specific properties, i.e. a narrow bandwidth due to the ionic character of the bonds, and a pronounced localization of conduction electrons resulting from the strong polarization of the bonds, lead to low carrier mobility and are in complete contradiction with traditional criteria for choosing good thermoelectric material. Also, the discovery of a high figure of merit in the Na_xCoO_2 compound [2] was a real surprise and the trigger for many studies on the thermoelectric properties of oxides. The Cobalt oxides with a lamellar structure or misfit, such as Na_xCoO_2, $Ca_3Co_4O_9$ and their derivatives compounds have been the subject of numerous studies, and present themselves as the best p-type oxide materials [3, 4, 5]. The work of Prevel [6], Lemonnier [7] and Kenfaui [8] have contributed to the improvement of thermoelectric properties of the bulk compound $Ca_3Co_4O_9$. In addition, a number of publications recently published [9, 10], state that another way can be taken to improve the thermoelectric properties of these materials.

Our study deals with elaboration and texturing of $Ca_3Co_4O_9$/Ag (349/Ag) composites by replacing cations Ca^{2+} cations by Ag^+ cations or by adding solid silver in $Ca_3Co_4O_9$ phase. The purpose of this approach is to take advantage of the metallic nature of silver, to reduce the resistivity, as well as allow increased power factor (PF) and to some extent improve the thermomechanical properties. To achieve our goal, we will make a synthesis of 349/Ag composite by solid state reaction of the precursors and using conventional sintering (CS), spark plasma sintering (SPS) and a new technique combining the SPS sintering and texturing called Spark Plasma Texturing (SPT) [11], then make a comparative study of thermoelectric properties to retain the optimum sintering method and the correct orientation for cutting of thermoelements.

2. Experimental

2.1. Synthesis

There are two methods commonly used to synthesize the

* Corresponding author:
jeromedikwa@gmail.com, jerome.dikwa@univ-ndere.cm (Jérôme Dikwa)
Published online at http://journal.sapub.org/ijme

powder used to develop massive ceramic $Ca_3Co_4O_9$: synthesis by a liquid process [12, 13] and synthesis by solidroute [14]. The synthesis by solid state reaction is the mostly used and the easiest method to implement. Precursors, i.e. $CaCO_3$ and Co_3O_4 powder form, are mixed under dry conditions, and the mixture thus obtained undergoes calcination to obtain the required $Ca_3Co_4O_9$ phase. Work carried out in the CRISMAT laboratory showed that this method is more suitable for optimization of $Ca_3Co_4O_9$ ceramic [6]. The choice of a mode over another is mainly influenced by the final properties desired. The control of the shape and size of the grains, through the synthesis method chosen, is one of the first steps needed to optimize solid materials $Ca_3Co_4O_9$.

A mass $m = 20\,g$ of $Ca_{2.7}Ag_{0.3}Co_4O_9$ powder was synthesized by conventional solid state reaction, from a mixture prepared by stoichiometric proportions of: $12.3416\,g$ of cobalt oxide Co_3O_4 [*AnalorNormapur-Prolabo*], $10.3878\,g$ of calcium carbonate $CaCO_3$ [*Cerac 99.95%*] and $1.2439\,g$ of Ag [*Chempur 99.9%*]. These precursors were mixed and milled in dry conditions, in a machine at planetary movement containing beads and set at $400\,rpm$ for $30\,min$. The mixture was finely crushed in a mortar, and then calcined at $920\,°C$ for 24 hours to promote the decomposition of carbonates; thereby obtaining the desired phase and finally, X-ray diffraction was carried out to ensure the phase. After calcination, we added solid Ag corresponding to $10\,wt\%$ of $Ca_{2.7}Ag_{0.3}Co_4O_9$; then the whole was ground again during $30\,min$ in the machine.

2.2. Shaping and Sintering

Before sintering, the crucial step is the shaping, enabling good cohesion of the grains and a better distribution of the material in order to eliminate the intergranular porosity. We use here three modes of sintering: conventional sintering (CS), Spark Plasma Sintering (SPS) and Spark Plasma Texturing (SPT).

2.2.1. Conventional Sintering (CS)

For the preparation of the bars; 4 drops of organic binder (polyvinyl alcohol, Rhodoviol to $5\,wt\,\%$ in an aqueous medium marketed by Prolabo) were added into $1.2\,g$ of powder. The mixture was then manually homogenized in the mortar, dried under epiradiator and disagglomerated before shaping. These organic binders can improve the flow ability of powders, for easy removal and offer at the preformed powder, sufficient mechanical strength before consolidation step at high temperature. We subdivided the mixture in $0.3\,g \times 4$ into uniaxial press mold and the press was set at $110\,mV$ and $44.5\,kN$. The bars were ultimately recovered and sintered at $920\,°C$ during $24\,h$, with an ascending and descending speed of $150\,°C/h$.

2.2.2. Spark Plasma Sintering (SPS)

We chose a graphite mold of diameter $\phi = 20\,mm$, a mass $m = 10\,g$ of 349/Ag, a temperature cycle having a rise of $450\,°C$ to 900 °C in $4\,min\,30\,sec$, a dwell temperature of 900 °C for $10\,min$ and a descent of $900\,°C$ to $450\,°C$ in $4\,min 30\,sec$. The pressure cycle is described as follows: a rise of $5\,kN$ to $16\,kN$ in $4\,min\,30\,sec$, a dwell pressure at $16\,kN$ for $10\,min$, and a descent of $16\,kN$ to $5\,kN$ in $4\,min\,30\,sec$. In the SPS configuration, where the powder is introduced directly into the mold (Figure 1 (a)), the residual pressure applied by the wall could hinder development, growth of platelets, and therefore, their alignment along a preferred direction. The performances of materials consolidated by SPS are lower than those of the samples obtained by the hot pressing (HP) process, although the relative density of the SPS samples reaches 99% [8]. To approach the HP configuration and reduce the texturing time of our materials, we propose a new SPS configuration, allowing free deformation of the material, which could promote the development and growth of platelets and their texturing. This new configuration is called Spark Plasma Texturing (SPT) [11], and the conventional configuration is commonly called Spark Plasma Sintering (SPS).

2.2.3. Spark Plasma Texturing (SPT)

Pre-sintered pellets are prepared using a mold of diameter $\phi = 16\,mm$ and a mass $m = 7.5\,g$ of 349/Ag powder, by uniaxial pressing (set at $100\,mV$ and $40.5\,kN$) and a pre-sintering under air, in a furnace set at a temperature of $800\,°C$ for 2 hours. After the phase of pre-sintering, we performed the texturing phase in the SPS device (Figure 1 (b)); the pre-sintered pellet is centered in a graphite mold, of diameter $\phi = 30\,mm$. The optimal diameter of graphite mold is about twice that of the pre-sintered pellet [8], in order to overcome the residual pressure applied by the wall, thus allowing free deformation of the sample and thus promoting growth and preferential orientation of platelets [11]. Temperature cycle is described as follows: an increase from $25\,°C$ to $900\,°C$ in $14\,min$, then a dwell temperature at 900 °C for 15 min and finally a descent from $900\,°C$ to $450\,°C$ in $4\,min\,30\,sec$. The pressure cycle is following: a constant pressure of $5\,kN$ in $14\,min$, a rise from $5\,kN$ to $35\,kN$ in $5\,min$, then a dwell pressure at $35\,kN$ for $10\,min$ and finally a descent from $35\,kN$ to $5\,kN$ in $4\,min\,30\,sec$. It should be noted here that we first reached, the dwell temperature before a rise in pressure to allow flow and prevent cracking of the pellet.

2.2.4. Stacking of "5-Layers"

The textured pellets have low thicknesses (about $2\,mm$) for consider their integration into thermoelectric generators (TEG), or their characterization in the direction parallel to the pressing axis. That is why we made the welding using the SPS device by stacking 5 monolayers of SPT pellets (Figure 2) in a graphite mold, with a diameter$\phi = 30\,mm$. The temperature cycle is such that, it rises from $450\,°C$ to $900\,°C$ in $4\,min\,30\,sec$, remains $10\,min$ at a dwell of $900\,°C$, then decreases from $900\,°C$ to $450\,°C$ in $4\,min\,30\,sec$, and finally cool back to room temperature. For pressure, it rises from $5\,kN$ to $10\,kN$ in $4\,min\,30\,sec$, stay $10\,min$ at $10\,kN$and finally decreases from $10\,kN$to $5\,kN$ in $4\,min\,30\,sec$. The final thickness of the stacking prepared was about $10\,mm$.

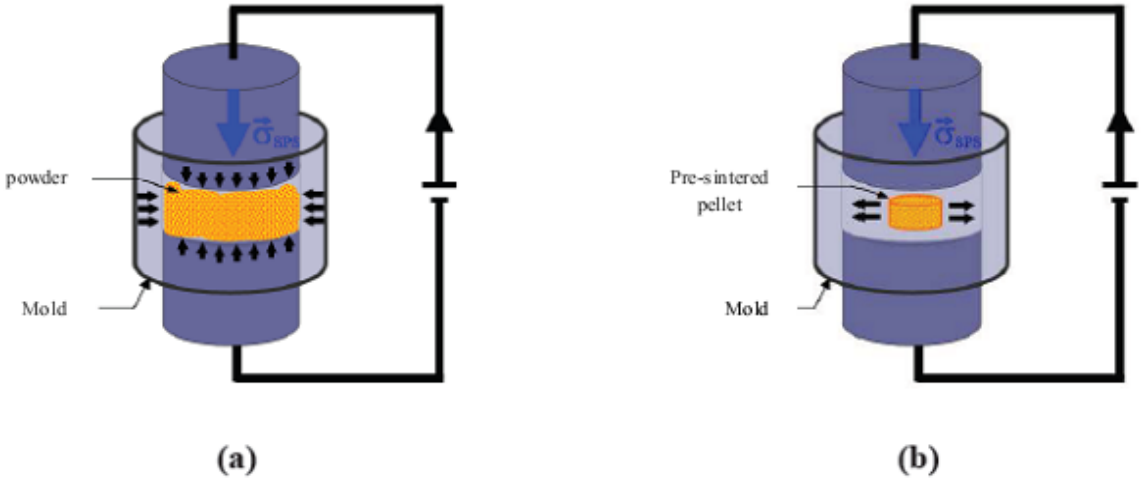

Figure 1. Diagrams illustrating the two SPS configurations used: (a) conventional configuration SPS and (b) new configuration 'SPT' for texturing a pre-sintered pellet [8]

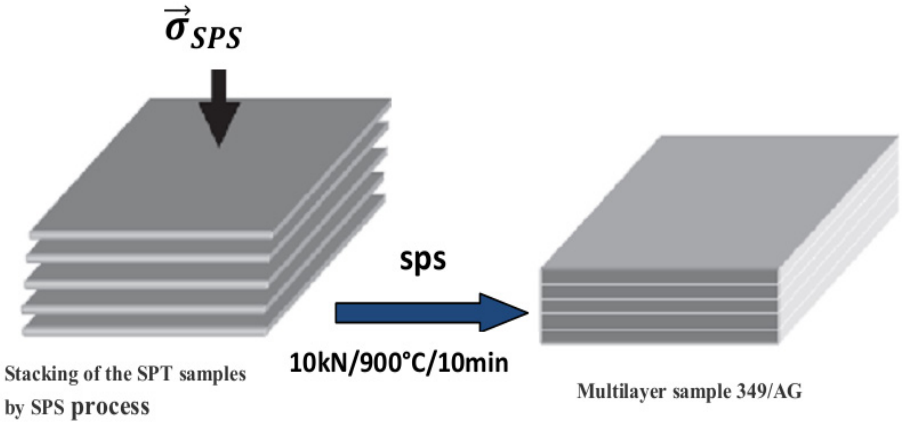

Figure 2. Development of a 5-layers stacking by SPS pressing of monolayer samples

2.3. Chemical and Structural Characterization

2.3.1. X-ray Diffraction

The devices used were, Xpert Pro MPD PANalytical (bla) and D8 Advance Vario 1 Bruker that may be used at high temperature, based on a Bragg-Brentano protocol $\theta - 2\theta$, whose main characteristic is the constant distance between the sample and the detector regardless of the angle θ. The interplanar distances are typical for each crystal. In addition, the relative intensity of the different peaks diffracted depends on the atoms in the lattice and their positions. One can determine precisely the different crystalline phases present in materials by comparing them with referenced phases in the XpertHighscore software. Lattice parameters can be determined accurately with software Jana 2006 [15]. This software uses Rietveld method [16] to accurately determine the lattice parameters of the crystal structure.

2.3.2. Scanning Electron Microscopy (SEM)

Microstructural studies were performed with a SEM Carl Zeiss (Supra 55, Oberkochen, Germany) and the observed samples have undergone different pre-treatments i.e. different polishing steps with abrasive discs. An electron beam produced by a field effect filament, scans the surface of the sample and detection of secondary electrons emitted, allows for production of the image. The number of secondary electrons depending on the inclination of the initial beam, at grazing incidence it is maximal. The sensor 'SE2' located in the room can see the contrast of the topography of the surface. Within the column, the detector 'in-lens' provides better resolution of image formed at the surface with electrons (low voltage, close to $5\,kV$ is required). It is possible to mix the contributions of these detectors, in order to optimize the image quality.

A third probe EDAX is added to the device; that makes it possible to capture emissions of X photons released by the sample irradiated with electrons. This method is called EDS or EDX (Energy Dispersive X-Ray Spectrometry). The energy of these photons is equal to the energy difference of two juxtaposed electron shells and is therefore characteristic of each atom. However, the photons energy dispersion is relatively large, resulting in a low resolution for low energy rays emitted by the atoms generally light. A quantitative analysis can be achieved for atoms with more than two electron shells.

2.4. Physical Characterizations

2.4.1. Measurements at High Temperature of the Resistivity and Seebeck Coefficient

We used the ZEM-3 apparatus (ULVAC- RIKO, Inc., Japan), to simultaneously measure the electrical resistivity and Seebeck coefficient at high temperature ($100 - 650\ °C$). The measurements were carried out under helium low pressure. Both ends of the sample were polished, so that they are parallel to ensure good contact with nickel electrodes of the device. The measuring chamber temperature is increased from room temperature to 650 °C, using an oven halogen controlled by temperature probes (YAMATAKE model SDC30) simultaneously measuring the sample temperature.

The device is provided with a precision current source (ADVANTEST model R6144) that can deliver a maximum current of about $160\ mA$, with a path length of $100\ nA$, and a multimeter (Keithley model 2010) to acquire voltages.

The programming of the measurement cycle at the ZEM-3 is performed by setting the different dwell temperatures desired (T_D) and the number of points measurement of the temperature between the steps. Typically, the dwell temperatures are selected every $50\ °C$ (T_D then $T_D + 50\ °C$) and three points are selected ($T_D + 10$, $T_D + 20$, $T_D + 30\ °C$) between two levels. The resulting difference in temperature between the two thermocouples in contact with the sample is of the order of 2 to $6\ °C$.

The Seebeck coefficient measurement is made by static, while the electrical resistivity is based on the four-probe method, with the application of direct current.

The sample is placed between two nickel electrodes and then whole is inserted between two blocks of alumina thermo stated at different temperatures. Two thermocouples are placed in direct contact with the sample for measuring the temperatures T_C and T_H respectively of the cold and hot sides. The potential difference, ΔV, induced by the presence of the temperature gradient $\Delta T = T_H - T_C$ created through the sample, is measured between the two thermocouples. The Seebeck coefficient is then calculated by the equation:

$$S = \Delta V / \Delta T \quad (1)$$

As for the electrical resistance, the measurement is performed in the same experimental setup, which is added to the application of a current I of known intensity along the sample through nickel electrodes. The measured voltage leads to the production of the resistance R of the sample by simply applying Ohm's law. If the section A of the sample and the distance L between the two points of measurement using thermocouples are known, we obtain the electrical resistivity:

$$\rho = RA / L. \quad (2)$$

The recorded measurements are then processed by software supplied with the device. This software allows extracting a single value of resistivity and Seebeck coefficient with dwell temperature.

2.4.2. Measurement of the Thermal Conductivity at High Temperature

The most widely used to determine the thermal conductivity at high temperatures is one the method by laser flash for measuring the thermal diffusivity that was developed in USA by G. L. Abbott [17]. In this technique, one side of a small sample is irradiated by a laser which heats it. The heat propagates through the material and elevating the temperature of the opposite surface is measured as a function of time by using an infrared detector (Figure 3).

The Thermal diffusivity, D, can be calculated from the thickness e of the sample and the time $t_{1/2}$, required to reach half of the maximum temperature increased.

Its expression is given by the equation [19]:

$$D = \frac{1{,}37\,.e^2}{\pi^2.t_{1/2}} = 0{,}1388.\frac{e^2}{t_{1/2}} \quad (3)$$

Note that the diffusivity is measured as a function of temperature T.

If the material density and specific heat are known, we can finally obtain the thermal conductivity, $\lambda\ (W.m^{-1}.K^{-1})$

$$\lambda = D.d.C_P \quad (4)$$

The density d was measured in case of this work with a device using the Archimedes method (KERN & Sohn GmbH, Baligen, Germany).

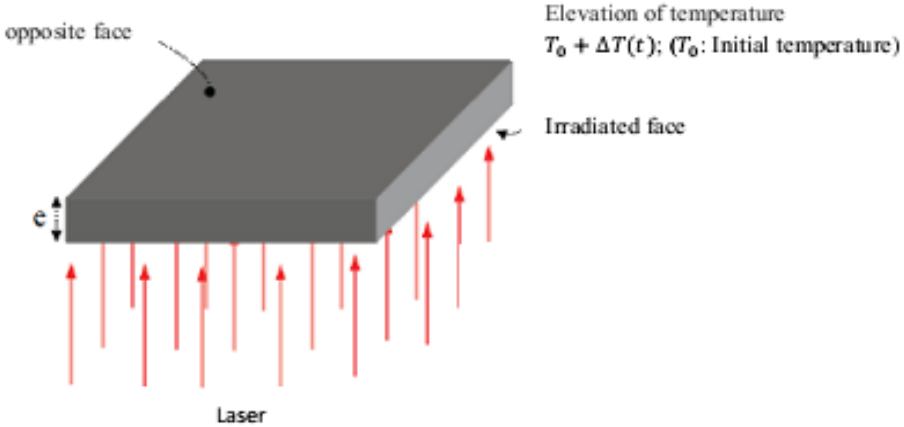

Figure 3. The flash laser method [18]

The heat capacity, C_P, is the energy required to raise $1\,°C$, the temperature of one gram or one mole of a material at constant pressure. It is defined by [20]:

$$C_P = \frac{dH(T)}{dT}.\frac{1}{m} \quad (5)$$

dH and dT refer to respective changes of the enthalpy and temperature. C_P was measured by differential scanning calorimetry (ATG/DSC STA 449 F3 Jupiter Netzsch, Selb, Germany) in case of this work.

Finally, the Dulong and Petit law [21] states that at high temperature, specific heat C_P of a solid tends to a constant value:

$$C_P = \frac{3.R}{M_M} \quad (6)$$

Where, $R(J.mol^{-1}.K^{-1})$ is the molar gas constant and $M_M(kg.mol^{-1})$ the molar mass of the material.

3. Results and Discussion

3.1. X-ray Diffraction of the $Ca_{2.7}Ag_{0.3}Co_4O_9$ Powder

Figure 4 shows the X-ray diffraction patterns of the $Ca_{2.7}Ag_{0.3}Co_4O_9$ powder compared with reference phases of $Ca_3Co_4O_9$ (349-REF), $Ca_9Co_{12}O_{28}$ (9 12 28-REF) and Ag-REF. This figure reveals that the phase obtained here is closer to the $Ca_9Co_{12}O_{28}$ (9 12 28) structure (with lattice parameters poorly known) and isostructural to $Ca_3Co_4O_9$ [14]. This shows that substitution of Ca^{2+}cations by heavier Ag^{+} cations causes distortion of lattice parameters. There is a lack of secondary phases, but rather the peaks corresponding to the phase of solid Ag indicating that the compound of formula $Ca_{2.7}Ag_{0.3}Co_4O_9$, is a composite compound. This hypothesis is confirmed by the SEM study coupled with EDS analysis of the $Ca_{2.7}Ag_{0.3}Co_4O_9$ powder.

3.2. The SEM Analysis Coupled with EDS Analyser of the $Ca_{2.7}Ag_{0.3}Co_4O_9$ Powder

Figure 5 shows the SEM image and the X mapping of O, Ca, Co and Ag elements in the $Ca_{2.7}Ag_{0.3}Co_4O_9$ powder. This figure reveals that the distributions of oxygen, calcium and cobalt are excellent, but we note the presence of precipitates (red spots) rich in solid silver; confirming that the compound is a composite.

3.2.1. Qualitative Study

From a qualitative standpoint, X maps were made to assess the homogeneity of the distribution of elements in the matrix. In general, we found that this is the $Ca_3Co_4O_9$ phase, with an extremely homogeneous distribution of O, Ca and Co elements constituent of the matrix. Regarding the Ag atoms inserted, we noticed the systematic presence of precipitates rich in Ag.

3.2.2. Quantitative Study

From a quantitative study, the chemical compositions obtained after data processing are not satisfactory because of certain areas highly concentrated in Ag.

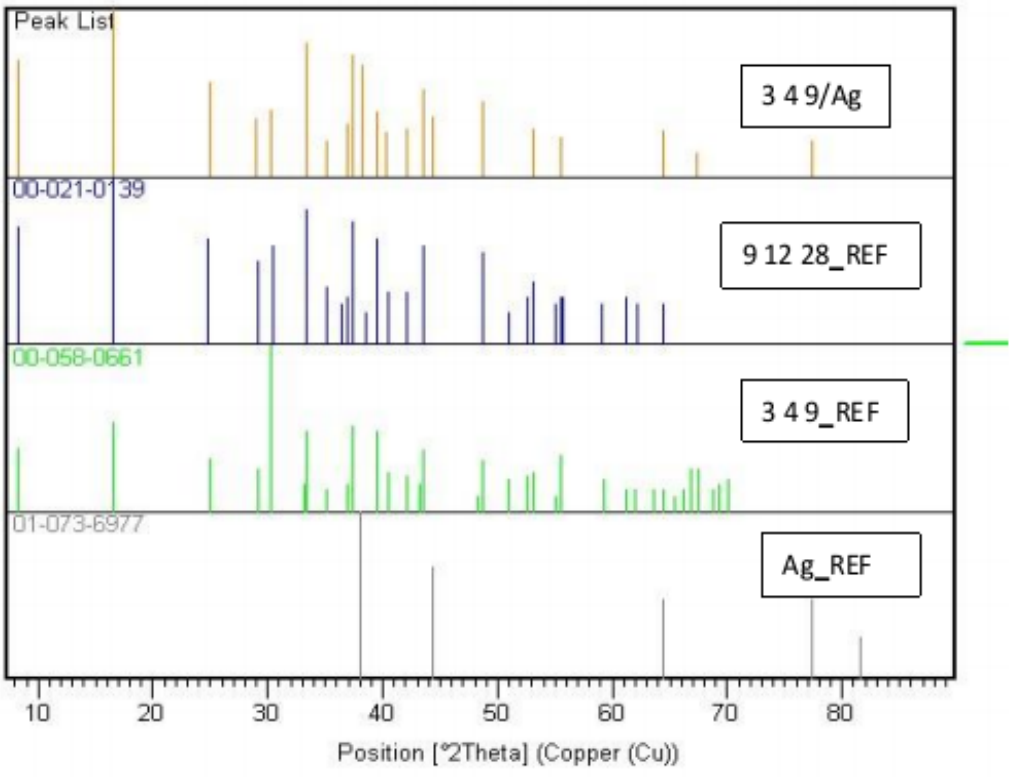

Figure 4. XRD patterns (Cu K_α radiation) of $Ca_{2.7}Ag_{0.3}Co_4O_9$ powder compare with XRD patterns of $Ca_9Co_{12}O_{28}$, $Ca_3Co_4O_9$ and Ag reference phases

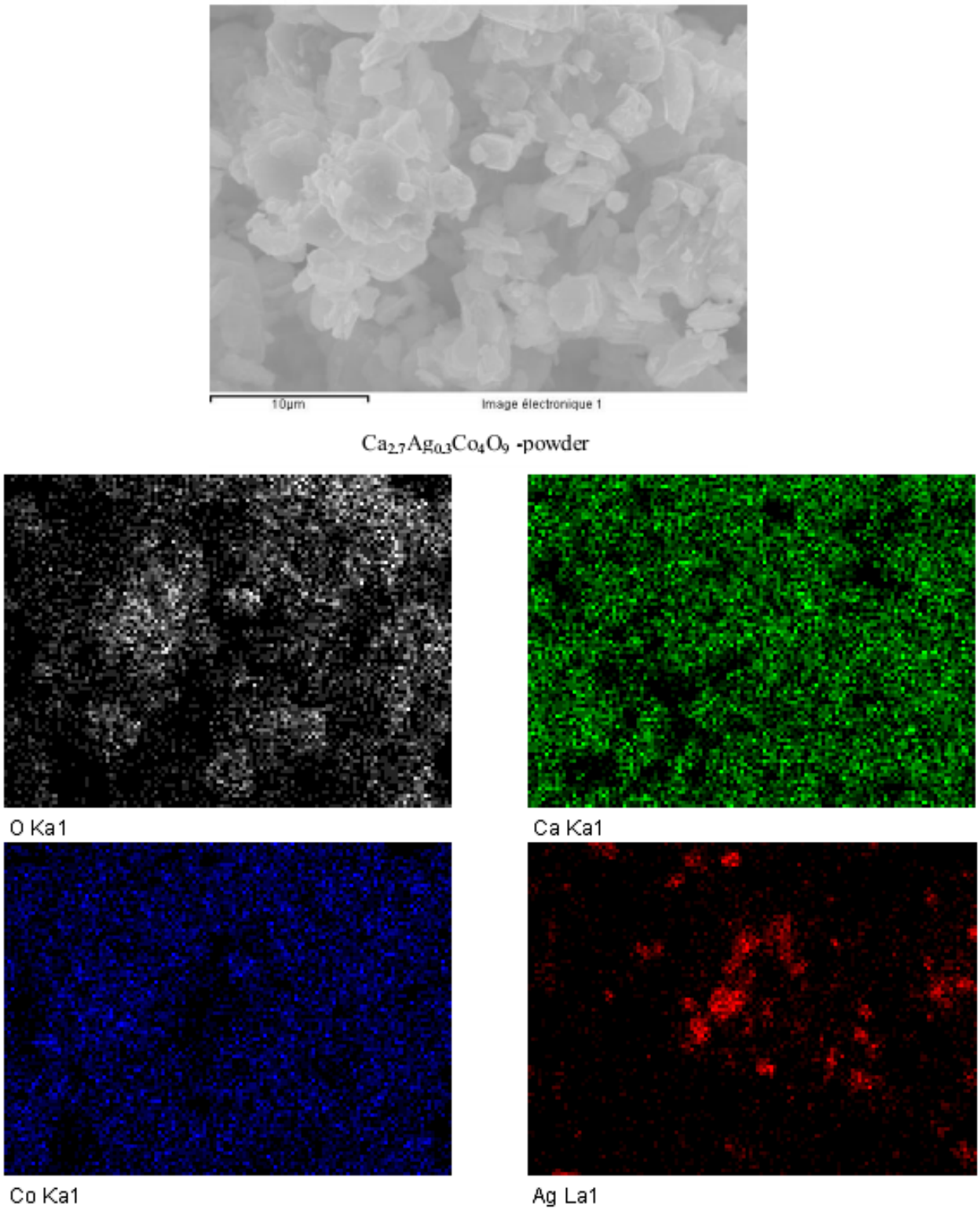

Figure 5. SEM image or backscattered electrons and X mapping of O, Ca, Co and Ag elements in the $Ca_{2.7}Ag_{0.3}Co_4O_9$ powder

3.3. Microstructure and Texture

Figure 6 shows the micrographs: **(a)** 349/Ag powder, **(b)** the sample of 349/Ag sintered conventionally, the fracture surfaces of samples prepared by the processes **(c)** SPS and **(d)** SPT. The observations were made in planes perpendicular to the pressing axis. This figure shows the evolution of the microstructure of the $Ca_3Co_4O_9$/Ag composite depending on the mode of sintering.

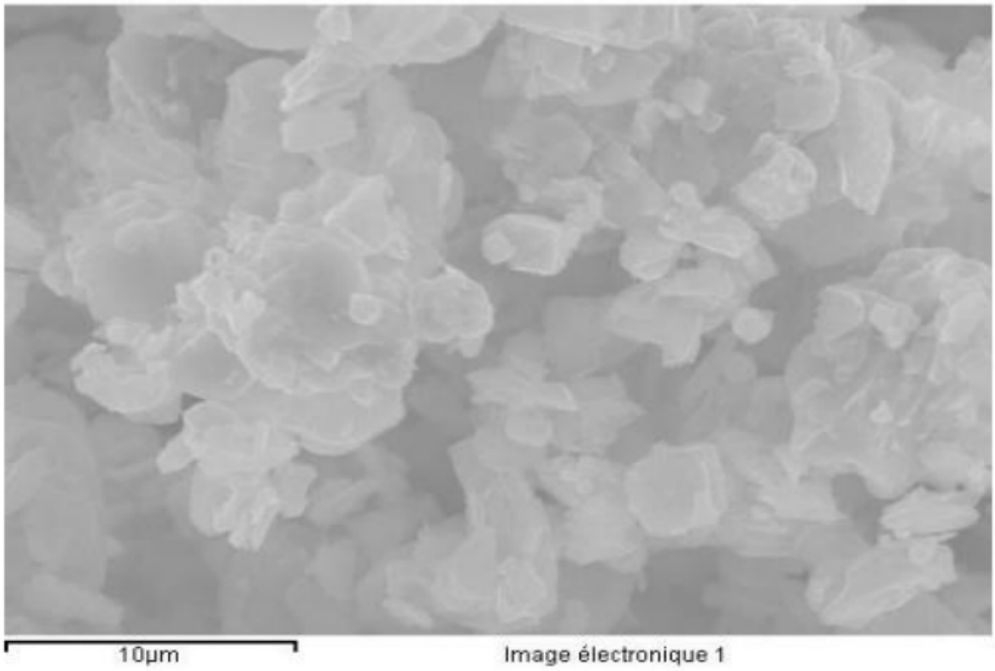

(a) 349/Ag-Powder

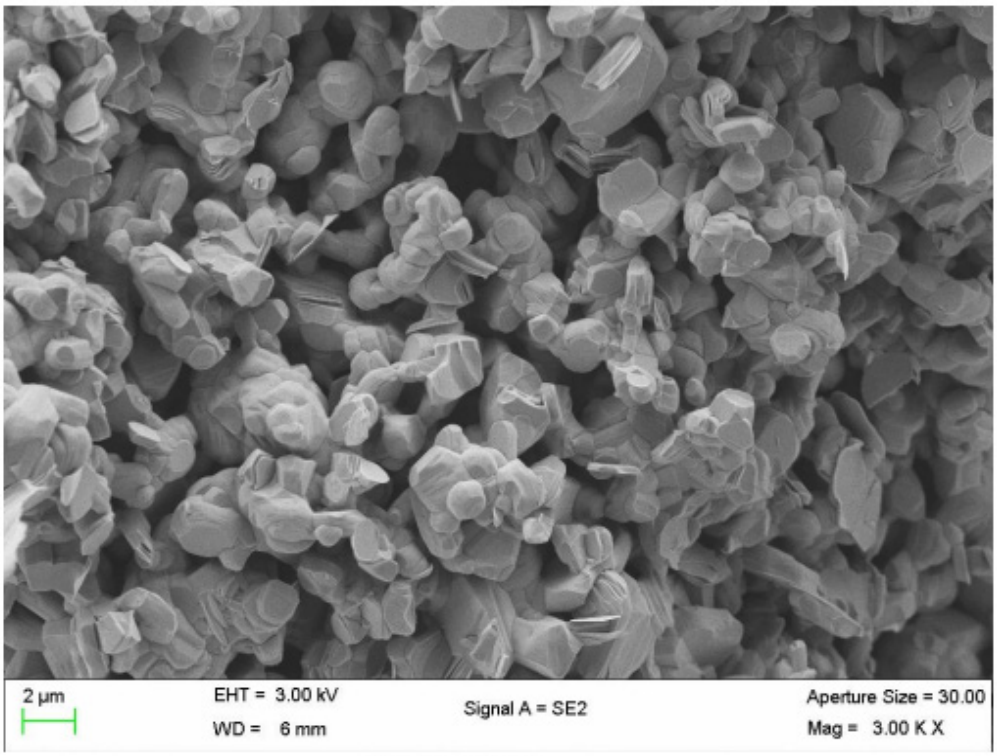

(b) 349/Ag-CS

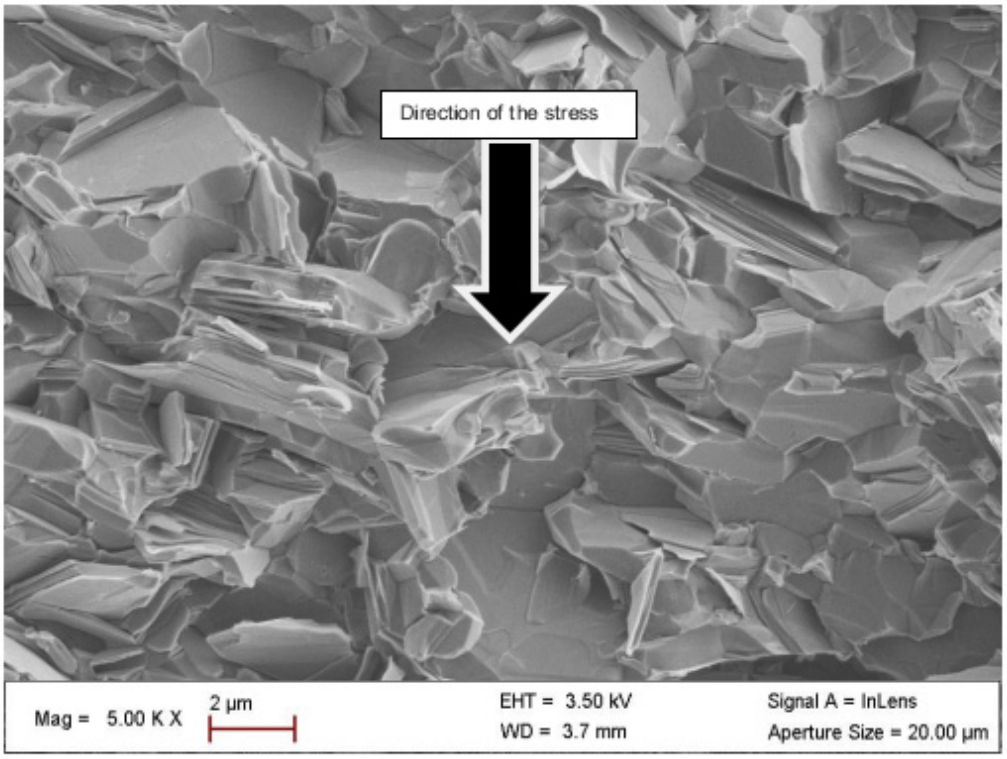

(c) 349/Ag-SPS_ab

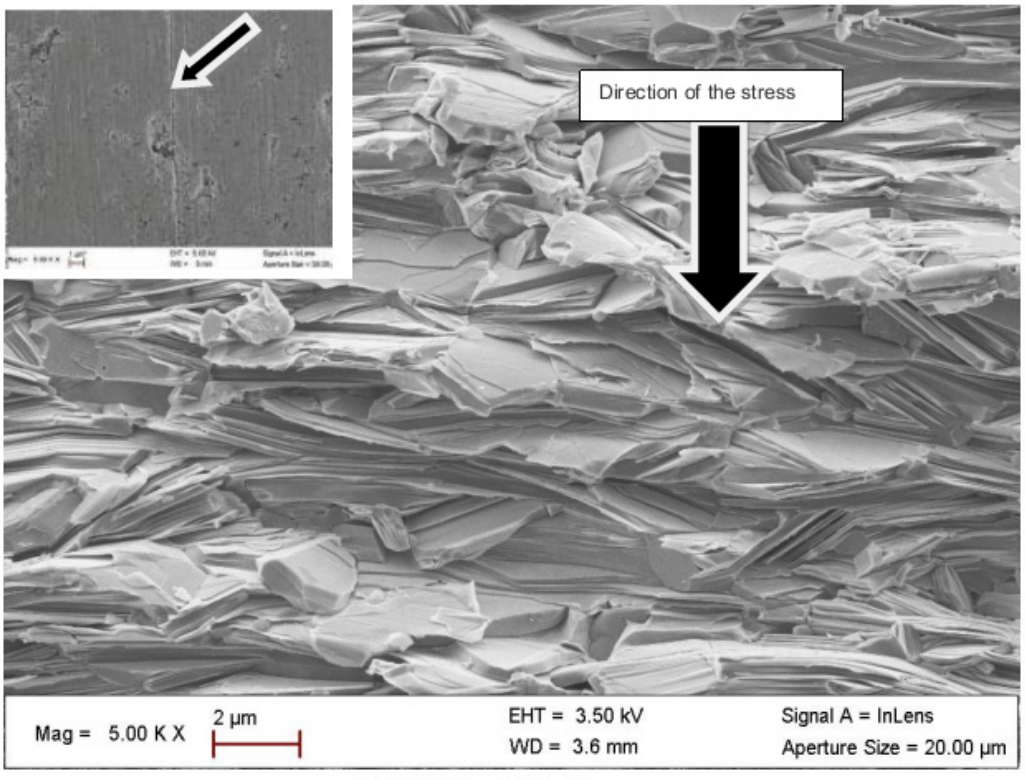

(d)349/Ag-SPT-ab

Figure 6. SEM micrographs, of the powder (**a**) and cross-sections of samples sintered by CS **(b)**, textured by SPS **(c)** and SPT_1-layer sample and insert the stack SPT_5-layers **(d)**

Figure 6**(b)** is an image obtained by scanning electron microscopy (SEM) on a cleaved surface of the sample sintered conventionally (349/Ag-CS). This material has small grains ($size \leq 5\,\mu m$) that appear randomly oriented and weakly assembled. We also note the presence of a large number of pores, which significantly reduces the density of the material and consequently, affects the various properties. The 349/Ag-CS relative density is estimated by Prevel [6], to be 60%.

Figure 6 **(c)** shows that the porosity is more eliminated, but no significant alignment of the grains is observed. The relative density is enhanced (99.6%) for dwell temperature of $900\,°C$; the grains are as platelets and the increase of their lateral size is not obvious ($\sim 9\,\mu m$). These limitations are likely explained by the additional lateral pressure applied to the sample by the walls of the matrix, whose effect is antagonistic to that of uniaxial pressure σ_{SPS} during sintering [11].

For the textured SPT sample (Figure 6 **(d)**), platelets are larger and reached their maximum lateral size $15\,\mu m$. The thickness of these platelets was therefore greatly reduced (below $0.12\,\mu m$). Porosity of this sample is reduced and consequently its relative density reaches 97.9%. We also notice a greater alignment of platelets that are distributed homogeneously and compact, along the pressing axis. These results highlight the reduction effect of the residual pressure applied by the wall in the SPT configuration. The space around the pre-sintered pellet (Figure 1 **b**) allows the latter to deform freely under the effect of the only uniaxial pressure, which promotes a more complete development of platelets and therefore, their growth. The rotation of these platelets is also done with less stress, thus leading to their orientation in the (a, b) planes.

For the SPT_5-layers sample, we could not distinguish any microcracks or separation line (interface) between monolayers at this level of magnification, which shows that the SPS treatment has permitted the shell to be welded together very well. A fine interface with an average width not exceeding $45\,nm$ is still observed at a much higher magnification on a polished section, as indicated by the arrow on the micrograph inset in figure 6 **(d)**. The relative density (~ 96.5%) is slightly affected in comparison with that of the original monolayer.

3.4. Thermoelectric Characterization

3.4.1. Comparative Study of the Thermoelectric Properties of 349 and 349/Ag

Figure 7 shows the temperature dependence of the resistivity of different samples. We clearly observe that the addition of silver helps to reduce the resistivity of one hand and on the other hand the new SPT configuration reduces the resistivity ρ^{ab} in the plane perpendicular to the pressing axis. This results in a significant decrease for the resistivity ρ^{ab} of the 349-Ag_SPT_1-layer sample. The value of ρ^{ab} is estimated to $2.65 \times 10^{-5} \Omega m$ at $630\,°C$ for the composite $Ca_{2.7}Ag_{0.3}Co_4O_9 + 10\,wt\%$ Ag (349/Ag); against a value of $9.3 \times 10^{-5}\,\Omega m$ for $Ca_3Co_4O_9$ ceramic sintered by SPS [8], this value corresponding to 71% decrease. We note: (i) a correlation between the reduction of the resistivity and the microstructural observations, and (ii) the decrease of ρ^{ab} when platelets are better aligned because of the availability of a space larger creep (larger diameter mold).

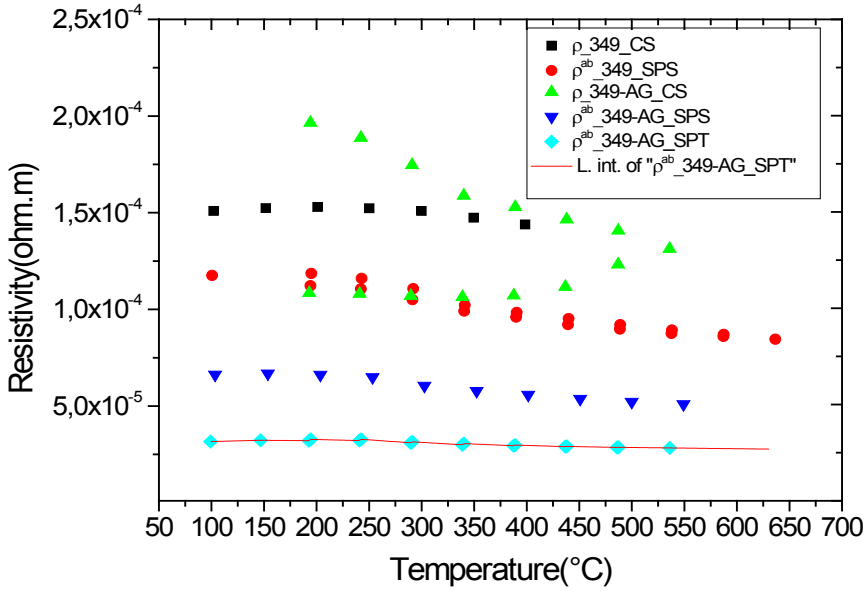

Figure 7. Evolution of the resistivity as a function of temperature for samples: 349_CS, 349_SPS, 349-Ag_CS, 349-Ag_SPS and 349-Ag_SPT_1-layer

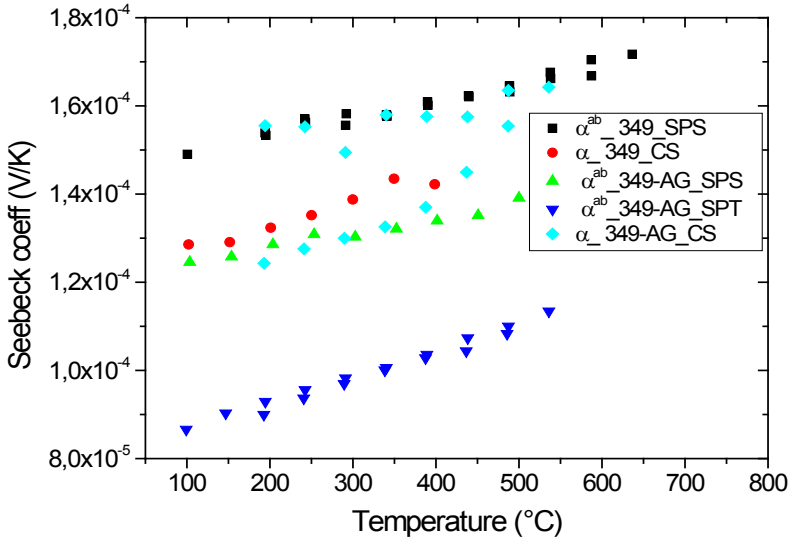

Figure 8. Temperature dependence of the Seebeck coefficient for the samples: 349_CS, 349_SPS, 349-Ag_CS, 349-Ag_SPS and 349-Ag_SPT_1-layer

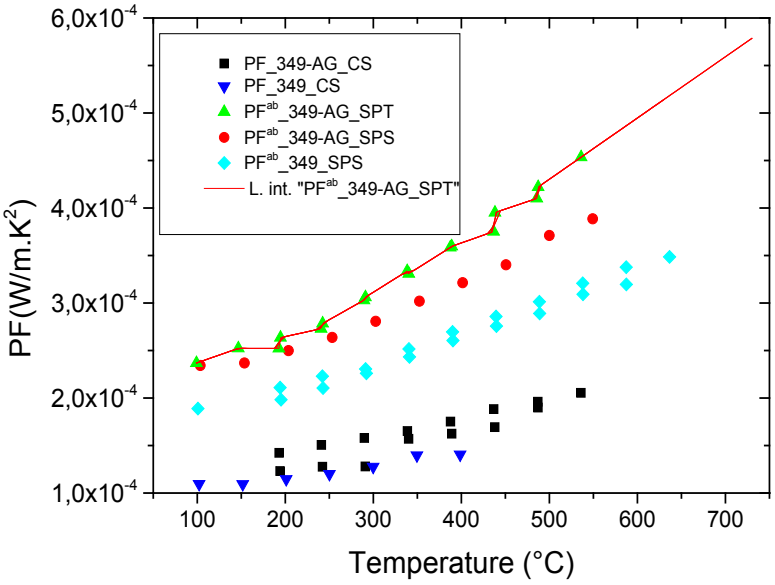

Figure 9. Temperature dependence of the power factor (*PF*) for the samples: 349_CS, 349_SPS, 349-Ag_CS, 349-Ag_SPS and 349-Ag_SPT_ 1-layer

Indeed, although it has a lower relative density 97%, the 349-Ag_SPT sample textured in a mold of $\phi = 30\ mm$ has values ρ^{ab} lower than the 349-Ag_SPS sample which also presents low values compared to the other samples. This can be explained by a higher lateral size of platelets and their better alignment; therefore, the effects offset the density difference observed between the two materials. The smaller values ρ^{ab} of the 349-Ag_SPT_1-layer sample resulting from its larger platelets which reduce the density of grain boundaries and in particular the higher texture to improve current flow in the (a, b) planes.

Figure 8 shows the temperature dependence of the Seebeck coefficient for the different samples. The Seebeck coefficient slowly increases with temperature. However, the addition of silver combined with texturing SPT seems unfavorable to the Seebeck coefficient due to the low thermopower of metallic silver. There is a decrease on the value of α^{ab}, from $177\mu V.K^{-1}$ for $Ca_3Co_4O_9$ textured by HP [8] to $153\ \mu V.K^{-1}$ for the 349-Ag_SPT_1 layer sample.

However, the reduction of ρ^{ab} it is more important than the degradation of α^{ab}, which significantly improves the power factor PF^{ab} (Figure 9).

Figure 9 shows that the power factor of the 349/Ag composite is improved, compared to the 349. Combined with the SPT texturing, adding silver helps to significantly improve the power factor PF^{ab}. For 349-Ag_SPT_1-layer sample, it reaches $555\ \mu W.m^{-1}K^{-2}$at $630\ °C$ ($\sim 900\ K$), against $404\ \mu W.m^{-1}K^{-2}$ at $900\ K$ for 349 _SPT_1-layer obtained by Kenfaui [8]; which correspond to an increase of about 37%. By extrapolation, the expected value is about

$600\ \mu W.m^{-1}K^{-2}$ at $730\ °C$ ($\sim 1000K$). This value is also higher than the value of $420\ \mu W.m^{-1}K^{-2}$ obtained recently by Madre et al [22], using the Electrically Assisted Laser Floating Zone (EALFZ) technique. This result shows the possibility of a much faster texturing with interesting values of PF^{ab} comparable to those obtained by HP [8]. The texturing time of sample sintered by the SPT process (~ 1 hour) is a major advantage, compared to 36 hours required by the HP process [8] or 72 hours needed for the EALFZ [22].

3.4.2. Study of the Anisotropy of the Thermoelectric Properties of 349/Ag Composites

3.4.2.1. Samples Preparation for Thermoelectric Measurements

To measure the resistivities (ρ^{ab} and ρ^{c}) and the Seebeck coefficients (α^{ab} and α^{c}), a series of bars was cut from the heart of the 5-layers sample following the directions parallel and perpendicular to the pressing axis of dimensions ($3\ x\ 3\ x\ 8\ mm^3$). Parallelepipeds of dimensions $6\ x\ 6\ x\ 2\ mm^3$ or $8\ x\ 8\ x\ 2\ mm^3$ were also cut following these directions for measuring thermal conductivity (λ^{c} and λ^{ab}). The measurements were carried out in high temperature ranges. The samples cut in parallel and perpendicular to the pressing axis with sufficient lengths were used to perform a detailed study of the anisotropy of thermoelectric properties. Measurements of resistivity ρ^{c}, Seebeck coefficient α^{c} and thermal conductivity λ^{ab}, are a very interesting challenge, because there are only very few results of similar measurements in the literature.

3.4.2.2. Electrical Resistivities (ρ^{ab} and ρ^{c}) and the Anisotropy Ratio of the Resistivity (ρ^{c}/ρ^{ab})

Figure 10 **(a)** represents the resistivity ρ^{c} following the pressing axis ($\vec{c}$) and the resistivity ρ^{ab} in the plane perpendicular to the pressing axis. The ρ^{ab} values of monolayer sample are also reported. The ρ^{ab} values of 5-layers sample are almost identical to those measured for a monolayer (ρ^{ab} is $2.82 \times 10^{-5}\Omega.m$ and $2.65 \times 10^{-5}\Omega.m$ at 900K respectively for 5-layers sample and 1-layer sample). These curves show that the temperature dependence of ρ^{c} is similar to ρ^{ab}, but the ρ^{c} values remain much higher. This is likely due partly to the increase in the density of the grain boundaries in the planes containing the $\vec{c}$ axis, that is the increase number of barriers to the electric current passage due to the remarkable reduction of the thickness of the grains under the effect of the σ_{SPT} pressure, and secondly, the texture rather favoring the current flow along the (a, b) planes. Another explanation may be suggested by considering the increasing number of interfaces in the 5-layers stack. At 900 K, the resistivity ρ^{c} is about $1.7 \times 10^{-4}\Omega.m$, value below those reported in the literature by Tani *et al.* [23] and Kenfaui [8] in the range $4.7 \times 10^{-4} - 5.6 \times 10^{-4}\Omega.m$ for 349. The ρ^{ab} curves have an inconspicuous transition around 450 K (see figure 10 (b)), which can be attributed to the spin transition [24] and the very low value $2.65 \times 10^{-5}\ \Omega.m$ of ρ^{ab} at 900 K for 349/Ag composite textured, is among the best reported in the literature.

Figure 11 shows the temperature dependence of resistivity anisotropy ratio ρ^{c}/ρ^{ab} of the 5-layers sample. The gap between ρ^{ab} and ρ^{c}, values means that there is anisotropy of the electrical resistivity. This anisotropy is expressed here by the ratio ρ^{c}/ρ^{ab}. Similar results were reported by Tani *et al.* [23], Zhang *et al.* [25] and Kenfaui [8] for the $Ca_3Co_4O_9$ ceramics textured by RTGG (Reactive Templated Grain Growth), SPS and SPT respectively. The anisotropy ρ^{c}/ρ^{ab} decreases with increasing temperature, as shown in figure 11. For the series of measurements, the average value of the ratio ρ^{c}/ρ^{ab} is about 6.4 at 900 K, lower than that reported by Tani *et al.* (7.25) [23] and Kenfaui (8.8) [8], but higher than that obtained by Zhang *et al.*(2.7) [25].

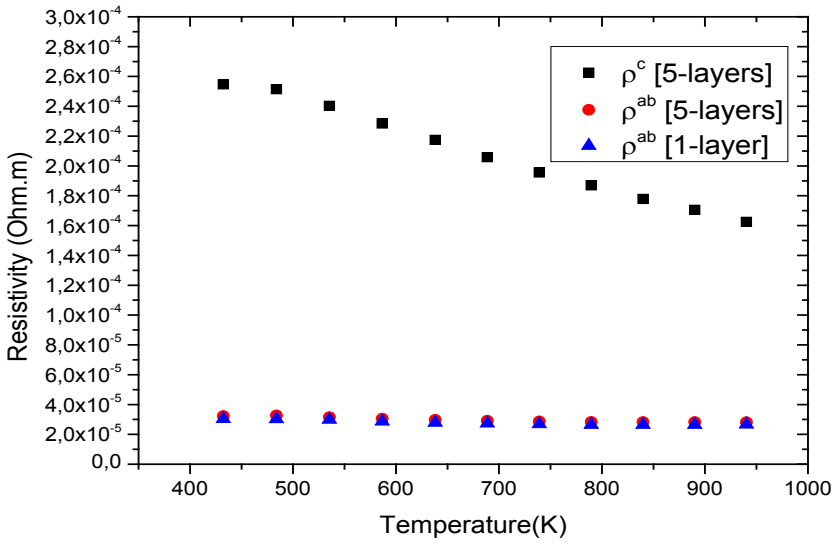

(a)

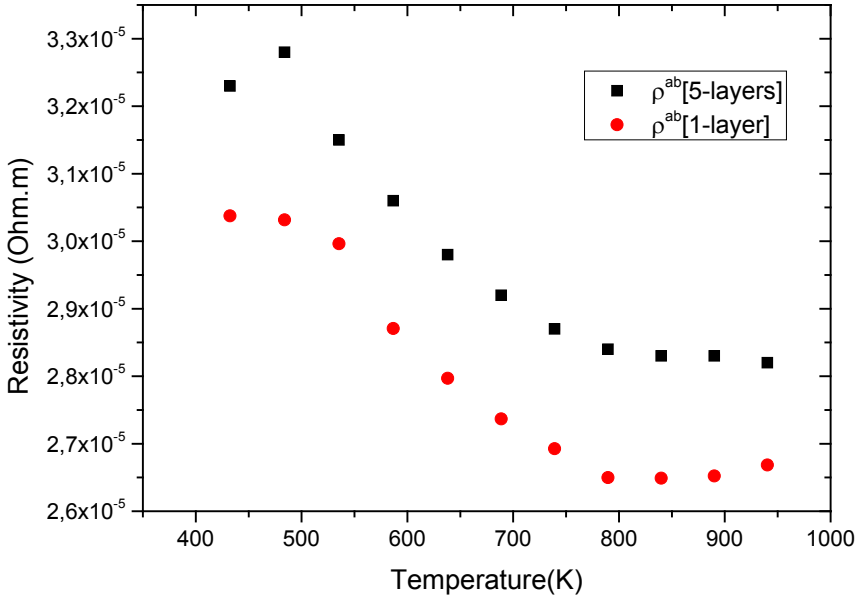

(b)

Figure 10. **(a)** Electrical resistivity as a function of temperature for thermoelements taken from the 5-layers sample along the parallel directions (ρ^c) and perpendicular (ρ^{ab}) to the pressing axis and the ρ^{ab} values of monolayer sample are also reported. **(b)** Electrical resistivity ρ^{ab} of 5-layers sample and 1-layer sample in large scale

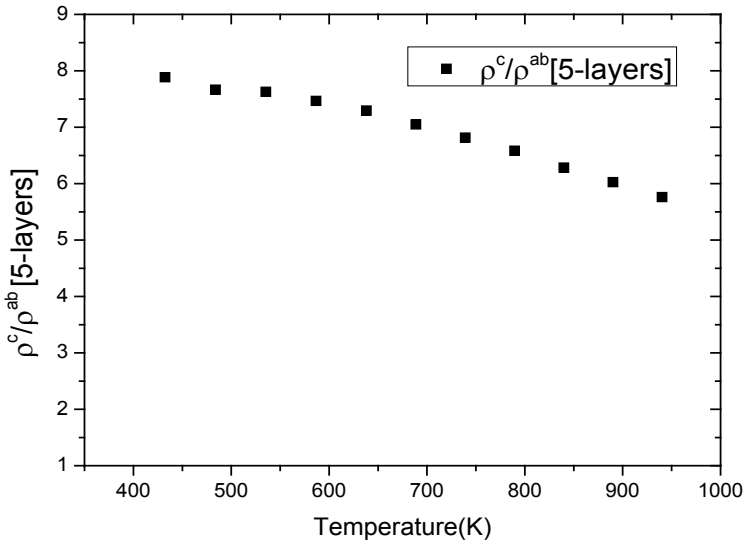

Figure 11. Temperature dependence of the anisotropy ratio of the resistivity (ρ^c/ρ^{ab}) of the 5-layers sample

3.4.2.3. Seebeck Coefficients (α^{ab} and α^c) and the Anisotropy Ratio of the Seebeck Coefficients (α^c/α^{ab})

Like the resistivity, the thermopower in the (a, b) planes and along the $\vec{c}$ axis was measured to verify the isotropic nature of this property. Figure 12 (a) shows the evolution of the Seebeck coefficient as a function of temperature, measurements being made along these two directions on the bars cut from the 5-layers stack. The α^{ab} values obtained for a monolayer are also reported. The α^{ab} curves have also a transition (hardly visible) around 450 K, which can be related to the spin transition [24]. The positive values of the Seebeck coefficient indicates that the majority charge carriers are positive (holes).

Figure 12 shows that the 5-layers stack has almost the same α^{ab} values as those of the monolayer. However, this

stack has α^{c} values slightly different and above those of α^{ab}. The difference $\alpha^{c} - \alpha^{ab}$ is about $14\,\mu VK^{-1}$, indicating an anisotropic character of the Seebeck coefficient. This result seems to disagree with the literature where the thermopower depends only on the chemical (concentration of charge carriers) of the material andwould bean isotropic property intrinsic to the crystals. Tani *et al*. [23] and Kenfaui [8] have reported a difference between α^{c} and α^{ab}, but they neglected the difference obtained and thus concluded that the Seebeck coefficient of their textured ceramics $Ca_3Co_4O_9$ are insensitive to the crystallites alignment and the microstructure.

The values of $\alpha^{c} > \alpha^{ab}$ show here that the addition of Ag and the effect of SPT favour entropy of charge carriers in the plane parallel to the $\vec{c}$ axis. Anyway, the difference is negligible and the Seebeck coefficient of the 349/Ag composite textured remains insensitive to the crystallites alignment and the microstructure.

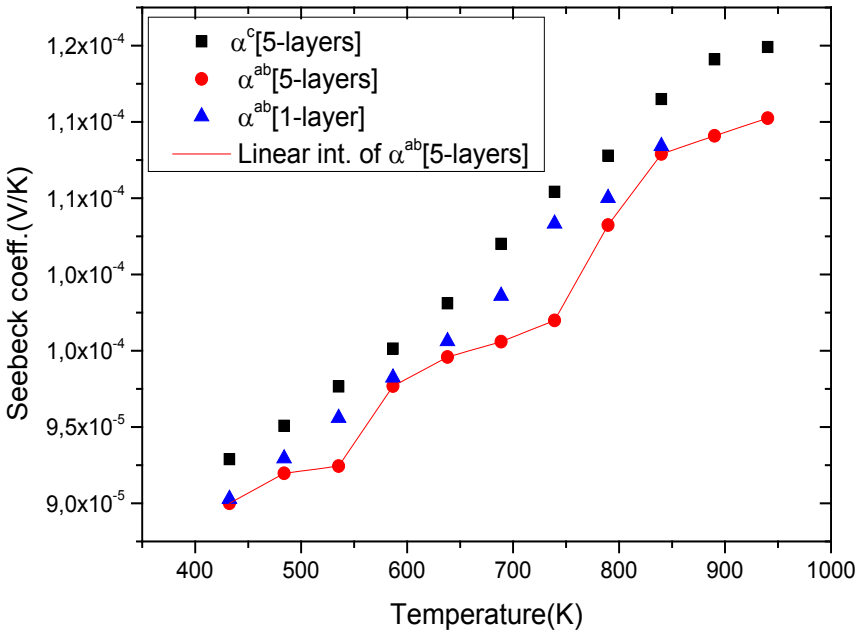

(a)

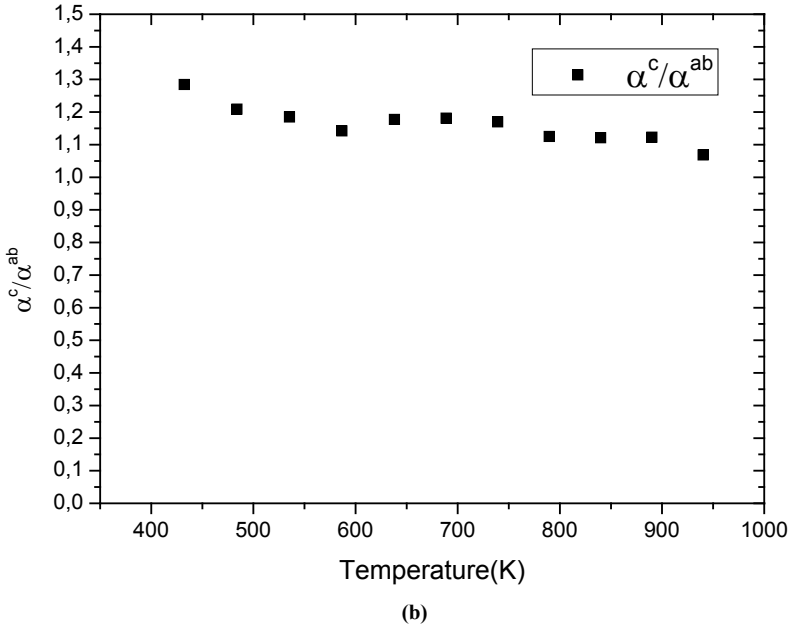

(b)

Figure 12. Seebeck coefficient as a function of temperature for bars taken from the 5-layers sample along the direction parallel (α^{c}) and direction perpendicular (α^{ab}) to the pressing axis. The values of α^{ab} 1-layer sample are also reported. **(b)** Illustration of the anisotropy ratio (α^{c}/α^{ab}) of Seebeck coefficient depending on the temperature

3.4.2.4. Power Factor (PF)

Figure 13 **(a)** presents changes of the resultant power factors as a function of temperature according to the directions parallel (PF^c) and perpendicular (PF^{ab}) to the pressing axis ($\vec{c}$) for the 5-layers sample. To facilitate comparison with the monolayer sample, the PF^{ab} values of monolayer sample are also reported. These PF^{ab} values are similar to those of the monolayer, but are much higher than those of PF^c. As values of the resistivity ρ^c are high relative to ρ^{ab} and those of the Seebeck coefficient α^{ab} slightly lower than α^c, the resultant power factor PF^c is much lower than that of PF^{ab}.

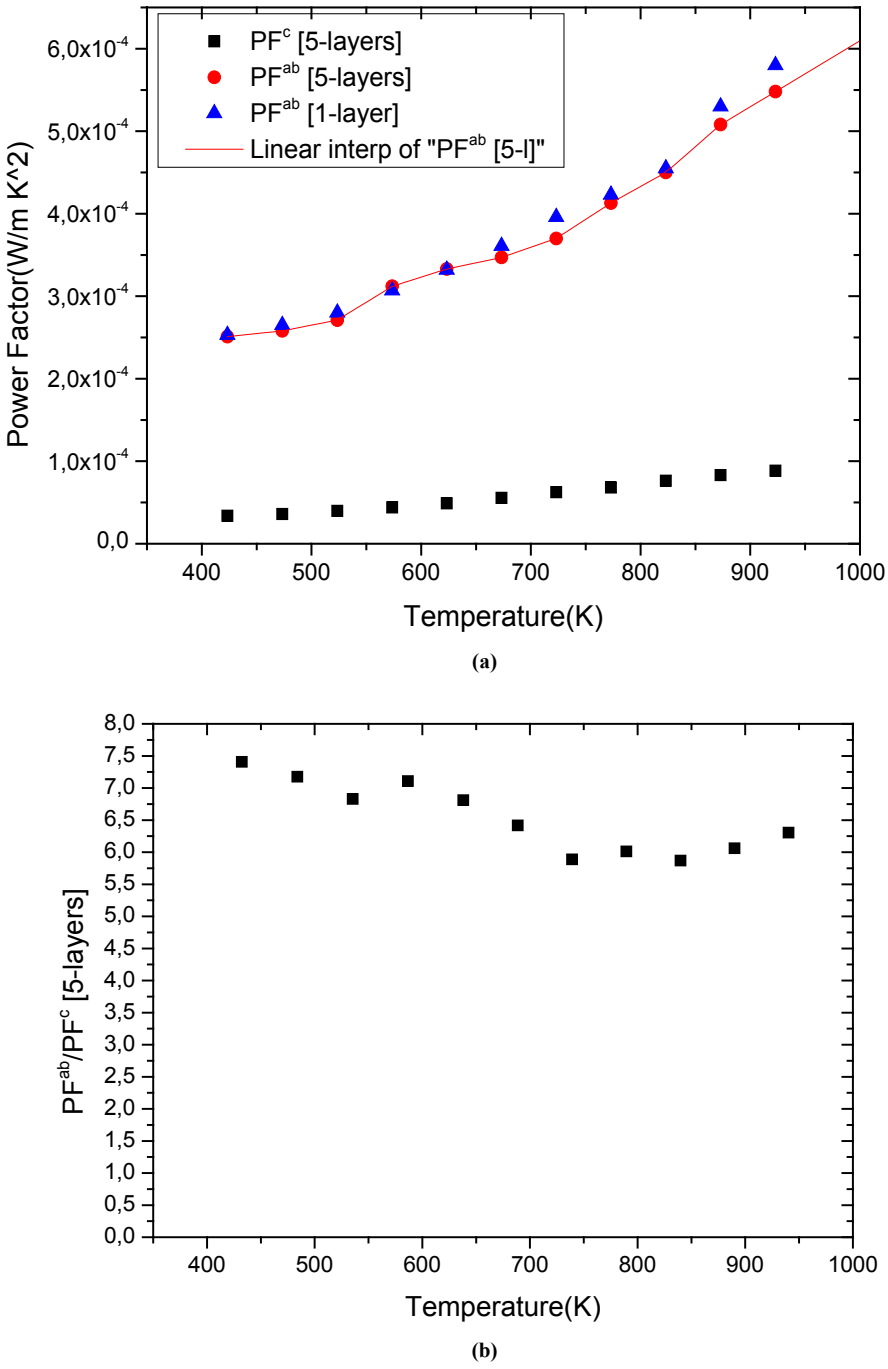

Figure 13. **(a)** Power factor as a function of temperature for bars taken from the 5-layers sample following the directions parallel (PF^c) and perpendicular (PF^{ab}) to the pressing axis. PF^{ab} values of the monolayer sample are also reported. **(b)** Changes of the anisotropy ratio (PF^{ab}/PF^c) of the power factor as a function of temperature

Moreover, the average values of anisotropy ratio of the power factor fall when temperature increases (Figure 13 **(b)**). At 900 K, the anisotropy ratio of the power factor is approximately 6 ($PF^{ab}/PF^{c} \sim 6$). The mean ratio PF^{ab}/PF^{c} obtained has decreased compared to that reported by Kenfaui on 349 textured by HP [8].

The values of $PF^{ab} = \frac{(\alpha^{ab})^2}{\rho^{ab}}$ are higher than those of $PF^{c} = \frac{(\alpha^{c})^2}{\rho^{c}}$ and are clearly improved for the 349/Ag_SPT sample. The PF^{ab} value reaches $524\,\mu W.m^{-1}.K^{-2}$ at 900K for the 349/Ag_SPT_5-layers sample. This value of $524\,\mu W.m^{-1}.K^{-2}$ at $900\,K$ is among the best in the literature [8, 22, 26, 27] for massive polycrystalline materials $Ca_3Co_4O_9$.

3.4.2.5. Thermal Conductivities (λ^{ab} and λ^{c})

Figure 14 **(a)** shows the temperature dependence of the thermal conductivity for 349/Ag_5-layers sample, following the directions parallel (λ^{c}) and perpendicular (λ^{ab}) to the $\vec{c}$ axis. The thermal conductivity λ can be expressed as the sum of electronic (λ_e) and lattice (λ_l) contributions, that is; $\lambda = \lambda_e + \lambda_l$. λ_e can be estimated from the Wiedemann-Franz law: $\lambda_e = L.\sigma.T = L.T/\rho$, where L is the Lorentz number ($L = 2.45 \times 10^{-8} V^2.K^{-2}$ for free electrons). λ_l is therefore obtained by subtracting ($\lambda_l = \lambda - \lambda_e$). Experimentally y, ρ^{ab} and ρ^{c} decrease with increasing temperature (Figure 10 (a)); therefore it comes from the Wiedemann-Franz formula, that λ_e increases with temperature. This shows that λ_l is the predominant component of the thermal conductivity in the $Ca_3Co_4O_9$/Ag system. These results are clearly verified for the thermal conductivities λ^{c} and λ^{ab} in figure 14 (b).

In addition, the lattice conductivity λ_l is proportional to the mean free path of the phonons, l_l, as stated in the following equation: $\lambda_l = \frac{1}{3} C_D v_l l_l$ where C_D is the lattice specific heat and group velocity v_l (equivalent to that of sound in the solid). Thus, reducing l_l implies that of λ_l. This, for example, is strongly present in nanocrystalline materials [28] due to phonon scattering by grain boundaries which density is very high.

In the case of conventional sintered sample for which the porosity is high (relative density is 60%) and grains are small ($5\,\mu m$), the density of barriers (pores and grain boundaries) that can influence the phonon scattering is very high. This significantly reduces the mean free path of phonons, l_l, and thus the lattice thermal conductivity λ_l of the material. The high electrical resistivity ρ also decreases the electronic contribution λ_e. This eventually results in a low thermal conductivity λ.

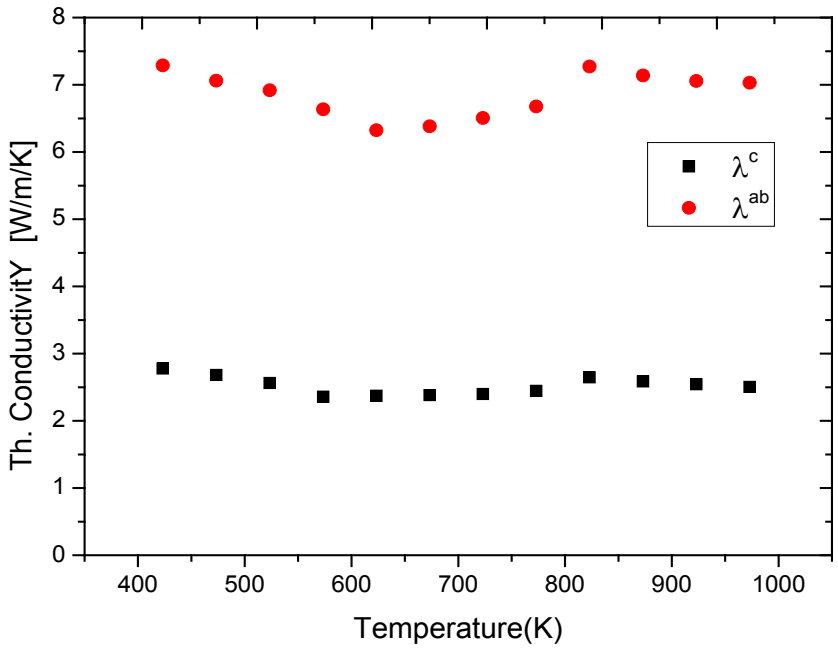

(a)

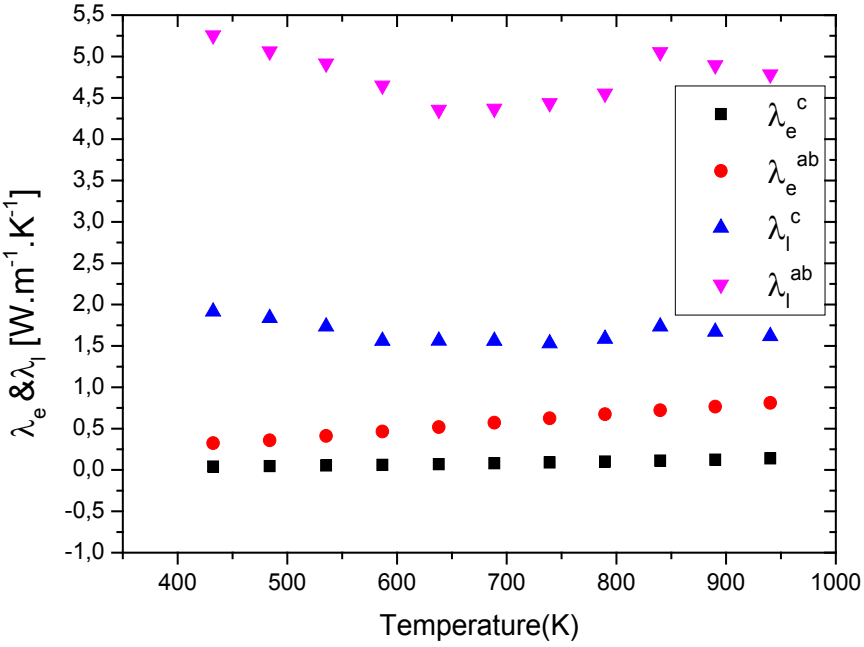

(b)

Figure 14. **(a)** Temperature dependence of thermal conductivities of 5-layers sample following the directions parallel (λ^{c}) and perpendicular (λ^{ab}) to the pressing axis. (b) Evolution according to the temperature of the electronic (λ_e) and lattice (λ_l) contributions to these thermal conductivities

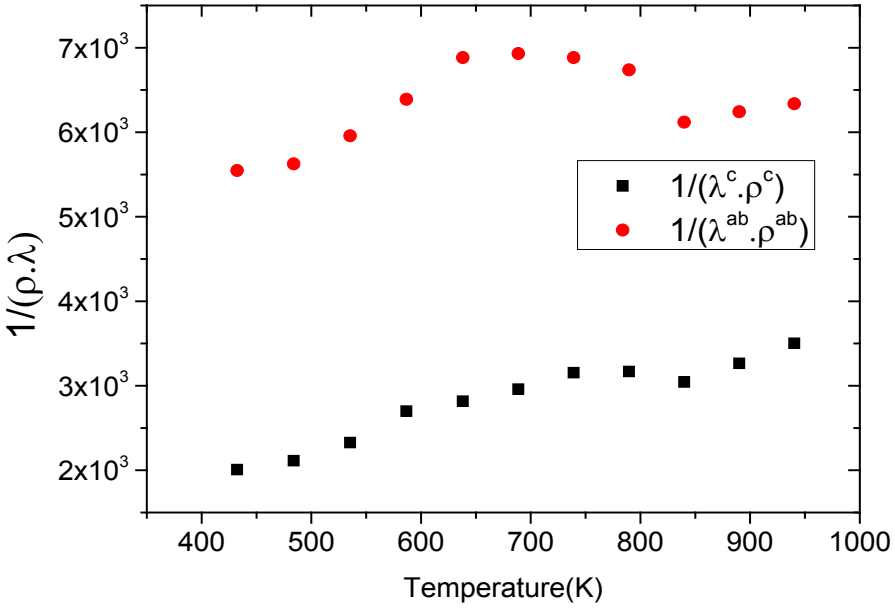

Figure 15. Variation of the ratio $1/(\lambda.\rho)$ as a function of temperature following the parallel and perpendicular directions to the $\vec{c}$ axis of the 5-layers sample

As for the 5-layers sample, the remarkable enhancement of its relative density compared to the CS sample is a primary factor in its high thermal conductivity. The thermal conductivity was measured according to the directions parallel and perpendicular to the $\vec{c}$ axis. The values of λ^{ab} are higher than those of λ^{c}. This difference is due to the crystalline anisotropy, texture and density difference induced by the grain joints following both directions during development. The lateral size of platelets significantly increased under the effect of SPT process ($15\,\mu m$), thus inducing a sharp decrease in the density of grain boundaries in the (a, b) planes, while their thickness was remarkably decreased ($\leq 0.12\mu m$), thereby increasing the density of grain boundaries in the planes containing the $\vec{c}$ axis. Finally, this results in the, influence of phonons scattering higher in the planes containing the axis of pressing than in the (a, b) planes. The mean free path l_l is lower in the planes containing the $\vec{c}$ axis and the lattice conductivity

$\lambda_l{}^c$ is therefore smaller than $\lambda_l{}^{ab}$. Their electronic conductivity $\lambda_e{}^c$ is less than $\lambda_e{}^{ab}$, due to their higher electrical resistivity ρ^c (Figure 10 **(a)**). The thermal conductivity λ^c is finally smaller than λ^{ab} which is also favored by thetexture [29].

At 900 K, the values of the thermal conductivities of the 5-layers sample are $\lambda^{ab} = 5.65\, Wm^{-1}.K^{-1}$ and $\lambda^c = 1.76\, Wm^{-1}.K^{-1}$, while the anisotropy ratio λ^{ab}/λ^c is 3.2.

This value of λ^{ab} is greater than that reported for single crystals ($3\, W.m^{-1}.K^{-1}$) by Shikano *et al.* [5]. It is also higher than values reported for the massive material by Wang *et al.* [30] ($1.96\, W.m^{-1}.K^{-1}$), Zhang *et al.* [31] ($1.6\, W.m^{-1}.K^{-1}$) and Kenfaui [8] ($3.1\, W.m^{-1}.K^{-1}$). This high value of λ^{ab} shows, that adding metallic silver is also favorable to the thermal conductivity.

In this study, we sought to improve the figure of merit ZT, by reducing the resistivity ρ. An immediate consequence is the variation of the thermal conductivity λ. Knowing that the Seebeck coefficient increases with temperature (Figure 12 **(a)**), the study of ZT as a function of temperature returns to explain the variation of $1/(\lambda.\rho)$. Figure 15 shows the dependence of this ratio with the temperature, in the directions parallel and perpendicular to the $\vec{c}$ axis, for 5-layers sample.

In the case of the 5-layers sample, the ratios $1/(\lambda^c.\rho^c)$ and $1/(\lambda^{ab}.\rho^{ab})$ evolve similarly with temperature while the ratio $1/(\lambda^c.\rho^c)$ is lower than $1/(\lambda^{ab}.\rho^{ab})$. Although λ^{ab} is above λ^c, values of $1/(\lambda^{ab}.\rho^{ab})$ are significantly higher than those of $1/(\lambda^c.\rho^c)$, due to the remarkable reduction of ρ^{ab} offsetting the increase in λ^{ab}.

It finally appears that our textured composites are much less resistive electrically and thermally in the (a, b) planes, than along the $\vec{c}$ axis.

The optimization of the ratio $1/(\lambda^{ab}.\rho^{ab})$ also involves reducing λ^{ab}, which requires more thermally resistive ceramic in their (a, b) planes. This can be produced by limiting grain growth during creep by SPT, which increases the density of grain boundaries favorable to the reduction of λ^{ab}. This reduction should be greater than the increase in ρ^{ab} which would be induced.

3.4.2.6. Figure of Merit

We present in figure 16: **(a)** figures of merit as a function of temperature for the 5-layers sample following the directions parallel (ZT^c) and perpendicular (ZT^{ab}) to the $\vec{c}$ axis, **(b)** A good fit of the curve $ZT^{ab}(T)$ using a second order polynomial and **(c)** The anisotropy ratio ZT^{ab}/ZT^c.

The increase of these figures of merit at high temperature, especially for ZT^{ab}, proves the performances stability at high temperatures, in addition to the thermal and chemical stability of these dense and textured materials. ZT^{ab} factors are higher than ZT^c ($ZT^c < ZT^{ab}$), which shows the predominance of the reduction of the resistivity for increasing ZT at high temperature.

At 900 K, ZT^{ab} is 0.082, with $ZT^{ab}/ZT^c \sim 1.8$ and the ZT^{ab} value reaches 0.10 at $1000\, K$, reflecting a conversion efficiency of polycrystalline textured $Ca_3Co_4O_9$/Ag much better along the (a, b) planes, than the planes containing the $\vec{c}$ axis and also with respect to the 349 sample textured by SPS [8]. This anisotropy ratio is lower than that obtained by Kenfaui [8] on the 349 ceramic textured by HP (4.6). HP process would be more effective to induce an improvement of thermoelectric performances of the $Ca_3Co_4O_9$ material and its derivatives, but this method is disadvantageous because it requires too long time texturing (36h) as compared to a shorter time texturing ($1\, h$) for the SPT. The estimated time for the elaboration of a 5-layers stacking sample is $202h$ by HP [8], against $4h$ for the SPT which is the technic used in our study; that is a gain in time of 98%.

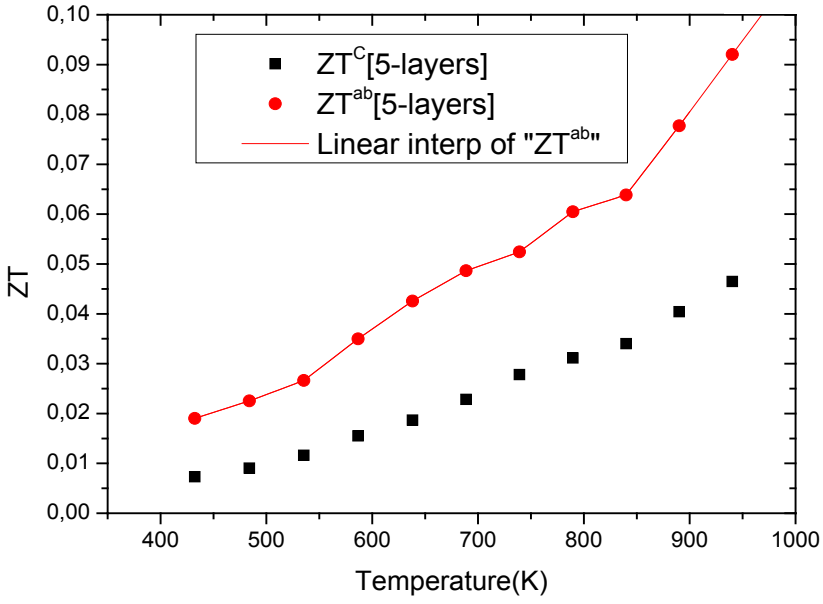

(a)

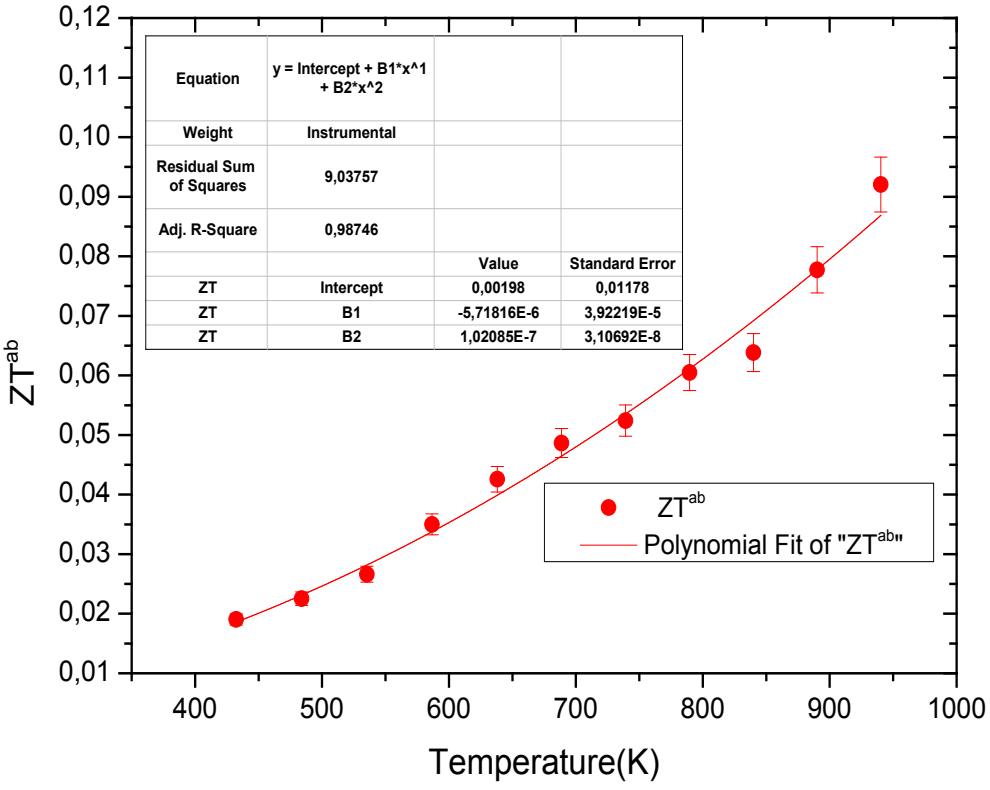

(b)

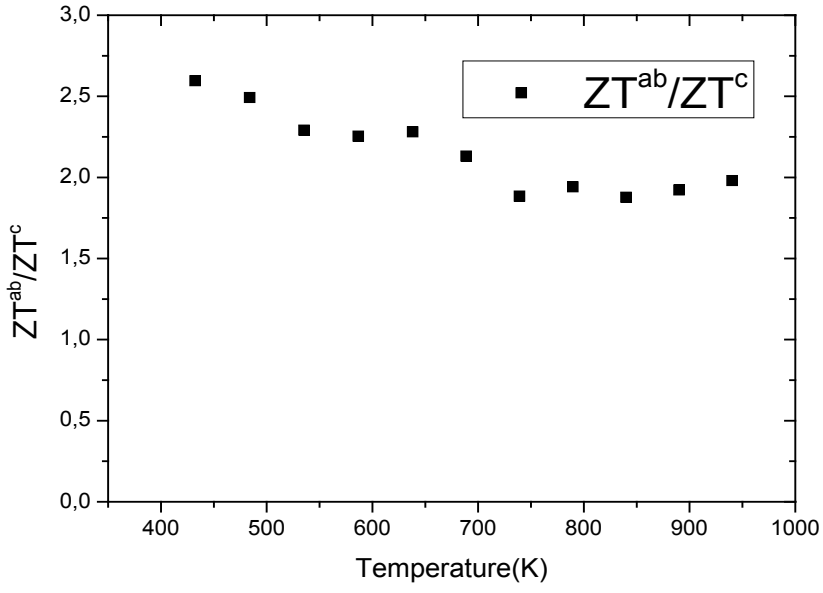

(c)

Figure 16. **(a)** Figures of merit as a function of temperature for the 5-layers sample following the directions parallel (ZT^c) and perpendicular (ZT^{ab}) to the pressing axis. **(b)** Curve fitting $ZT^{ab}(T)$ by a second degree polynomial. **(c)** The anisotropy ratio ZT^{ab}/ZT^c

4. Conclusion

Upon completion of this work, the $Ca_3Co_4O_9$/Ag composite ceramics have been elaborated using conventional sintering (CS), spark plasma sintering (SPS) and spark plasma texturing (SPT) process. The $Ca_3Co_4O_9$ (349) ceramics have been also elaborated by conventional sintering (CS) and spark plasma sintering (SPS). A comparative study of thermoelectric properties of different samples was performed. We have obtained a net reduction of ρ^{ab} in the $Ca_3Co_4O_9$/Ag composite sample textured by SPT, as a consequence of the substitution of Ca^+ cations by Ag^+ cations

and the addition of solid Ag, on one hand, and the effect of the SPT, on the other hand. The $Ca_3Co_4O_9$/Ag compound has a similar behavior to that of $Ca_3Co_4O_9$. The resistivity ρ^{ab} is $2.65 \times 10^{-5}\ \Omega.m$ at $900\ K$ for the composite. Adding Ag combined to the SPT process seems unfavorable to the Seebeck coefficient, due to the low thermopower of metallic silver; that resulted in $\alpha^{ab} = 153\ \mu V K^{-1}$ at $900\ K$. However, the reduction of ρ^{ab} is more important than degradation of α^{ab}, which significantly improves the power factor PF^{ab}: a remarkable value of $555\ \mu W.m^{-1}.K^{-2}$ is obtained at 900 K. Dense and textured pellets obtained by SPT are of small thicknesses to be considered studying their anisotropy and their integration into thermoelectric generator.

Indeed, multilayer pellets were successfully developed and have performances identical to those of monolayers textured samples. Thick samples thus prepared were of sufficient size for the study of anisotropic properties and allow cutting thermoelements adapted to the manufacture of thermoelectric generators.

The thermoelectric properties in the (a, b) planes remained unchanged after assembling monolayers. A decrease in the resistivity ρ^c is noted. The Seebeck coefficient α^{ab} proved insensitive to texturing. The power factor PF^{ab} is therefore much higher than PF^c, but similar to that of a monolayer.

The thermal conductivity is governed by the phonon contribution λ_l which is sensitive to the porosity, the density of grain boundaries, and texture. The values of the thermal conductivity also exhibit anisotropy, with $\lambda^c < \lambda^{ab}$.

The best values of the figure of merit at high temperature were obtained in the (a, b) planes, they are significantly higher than those measured on the sintered samples conventionally (CS) and SPS.

The new configuration 'Spark Plasma Texturing' (SPT) combining the benefits of SPS and oriented nature of the HP for a time saving of about 36 times compared to the HP conventional technique was effective for the development of samples very dense, (98% of theoretical density) textured, and efficient.

Moreover, due to the ductile nature of the Ag metal, we also expect an improvement in the thermomechanical properties of the $Ca_3Co_4O_9$/Ag composites, depending on thermal cycles, compared to $Ca_3Co_4O_9$ ceramics.

ACKNOWLEDGEMENTS

Jérôme DIKWA and the co-authors acknowledge Mr Alexandre WAHL for responding to the realization of this work on the CRISMAT lab. The authors thank also the CRISMAT Functional Materials and Structure (FMS) group for their help during the samples preparation and especially Mr Jérôme Lecourt during the powders synthesis and pellets sintering.

REFERENCES

[1] Rowe C. B. D. M., Modern Thermoelectric, 1st ed. Reston Publishing Company, Inc., Virginia, 1983.

[2] Terasaki I., Sasago Y., Uchinokura K., Phys. Rev. B, 1997, 56, R12685-R12687.

[3] Funahashi R., Matsubara I., Ikuta H., Takeuchi T., Mizutani U., Sodeoka S., Jpn. J. Appl. Phys., 2000, 39, L1127-L1129.

[4] Shikano M., Funahashi R., App Phys. Lett., 2003, 82, 1851-1853.

[5] Okuda T., Nakanishi K., Miyasaka S, Tokura Y., Phys. Rev. B, 2001, 63, 113104.

[6] Prevel M., Lemonnier S., Klein Y., Hébert S., Chateigner D., Ouladdiaf B., Noudem J. G., J. Appl. Phys., 2005, 98, 93706-93709.

[7] Lemonnier S., Thèse de doctorat de l'université de Caen, 17 octobre 2008, Caen.

[8] Kenfaui D., Thèse de doctorat de l'université de Caen, 09 mars 2010, Caen.

[9] Wang Y., Sui Y., Cheng J., Wang X., Su W., J. Phys : Condens. Matter, 2007, 19, 356216-356226.

[10] Zhang F.P., Lu Q. M., Zhang J. X., Zhang X., J. AlloysCompd., 2009, 477, 543-546.

[11] Noudem J. G., J. Eur. Ceram. Soc., 2009, 29, 2659-2663.

[12] Nagahama D., Tani T., Masuda Y., Itahara H., Yonesawa T., Koumoto K., 21st Int. Thermoelectr. Proc., Long Beach, 2002.

[13] Robert R., Romer S., Reller A., Weidenkaff A., Adv. Eng. Mat., 2005, 7, 303-308.

[14] Li S., Funahashi R., Matsubara I., Ueno K., Yamada H., J. Mater. Chem., 1999, 9(8), 1659-1660.

[15] Petriek V., Dusek M., Palatinus L. Jana 2006.The Crystallographic Computing System, Institute of Physics, Praha, Czech Republic, 2006.

[16] Rietveld H. M., Acta Crystallographica, 1967, 22(1), 151-152.

[17] Parker W. J., Jenkins R. J., Butler C. P., Abbott G. L., J. Appl. Phys., 1961, 32, 1679.

[18] Rowe D. M., Thermoelectrics Handbook, Macro to Nano, CRC Press, Boca Raton, FL, 2006, p. 58-1 – 58-21.

[19] Taylor R., in CRC Handbook of thermoelectrics, In: D. M. Rowe (Ed.), CRC Press, Boca Raton, Florida, 1995, p.165.

[20] Tari A., The Specific Heat of Matter at Low Temperatures, Imperial College Press, London, 2003.

[21] Petit A. T., Dulong P. L., Annal. Chim. Phys., 1819, 10, 395.

[22] Madre M. A., Costa F. M., Ferreira N. M., Sotelo A., Torres M. A., Constantinescu G., Rasekh Sh., Diez J. C., J. Eur. Ceram. Soc., 2013, 33, 1747-1754.

[23] Tani T., Itahara H., Xia C., Sugiyama J., J. Mater. Chem., 2003, 13, 1865-1867.

[24] Reddy E. S., Noudem J. G., Hébert S., Goupil C., J. Phys. D: Appl. Phys., 2005, 38, 3751-3755.

[25] Zhang Y., Zhang J., Lu Q., Ceram Int., 2007, 33, 1305-1308.

[26] Chateigner D., ed. Combined analysis: structure-texture-microstructure-phase-stresses reflectivity analysis by X-ray and neutron scattering, ISTE, London, 2010 p. 335. [online] Available at http://www.ecole.ensicaen.fr/~chateign/texture/combined.pdf (July 12, 2012)

[27] Behnia K., Jaccard D., Flouquet J., J. Phys. Condens. Matter., 2004, 16, 5187-5197.

[28] Nolas G. S., Sharp J., Goldsmid H. J., Thermoelectrics, Basic principles and new materials developments, Springer, New York, 2001.

[29] Mikami M., Guilmeau E., Funahashi R., Chong K., Chateigner D., J. Mat. Res., 2005, 20 (9), 2491–2497.

[30] Wang D., Chen L., Wang Q., Li J., J. Alloy. Compd., 2004, 376, 58-61.

[31] Zhang Y., Zhang J., J. mater. Proc. Technol., 2008, 208, 70-74.